

## Article

# Numerical Investigation of Electro-Thermal Field Distribution Law of Busbar under Different Operating Conditions

Wenyuan Hou <sup>1,2</sup> , Kaibing Sun <sup>1</sup>, Shuaigeng Sun <sup>2</sup> and Mao Li <sup>2,\*</sup>

<sup>1</sup> School of Energy and Power Engineering, North University of China, Taiyuan 030051, China; 20220047@nuc.edu.cn (W.H.); sunkaibing@nuc.edu.cn (K.S.)

<sup>2</sup> School of Energy Science and Engineering, Central South University, Changsha 410083, China; 213911032@csu.edu.cn

\* Correspondence: lmao@mail.csu.edu.cn

**Abstract:** The electro-thermal state of a busbar system of electrolysis cells for aluminum production represents the main factor affecting hydromagnetic stability and current distribution. Based on the busbar system of a 500 kA aluminum electrolytic cell, an overall busbar electro-thermal field coupling calculation model was established based on ANSYS. The characteristics of busbar temperature, current density, and voltage drop distribution were analyzed. In addition, the electro-thermal distribution of the busbar system was simulated under different current intensities, ambient temperatures, and heat transfer coefficients. The results show that the temperature distribution of the riser busbar and the cathode busbar is higher in the middle location and tends to decrease along the two sides. Differences in heat conduction and heat dissipation environment are the main factors affecting the distribution of the busbar system's electro-thermal field, while the Joule heat of the current is not the major factor. Increasing the current intensity will increase the average temperature and average voltage drop of the busbar. With an increase in the ambient temperature, the average busbar temperature increases significantly, and the voltage drop of the busbar also increases. With an increase in heat transfer coefficient, the average temperature and voltage drop of the busbar decreases.

**Keywords:** aluminum electrolytic cell; busbar system; electro-thermal field; numerical simulation



**Citation:** Hou, W.; Sun, K.; Sun, S.; Li, M. Numerical Investigation of Electro-Thermal Field Distribution Law of Busbar under Different Operating Conditions. *Metals* **2023**, *13*, 1361. <https://doi.org/10.3390/met13081361>

Academic Editor: David M. Bastidas

Received: 30 June 2023

Revised: 26 July 2023

Accepted: 27 July 2023

Published: 28 July 2023



**Copyright:** © 2023 by the authors. Licensee MDPI, Basel, Switzerland. This article is an open access article distributed under the terms and conditions of the Creative Commons Attribution (CC BY) license (<https://creativecommons.org/licenses/by/4.0/>).

## 1. Introduction

Aluminum electrolysis is an industry with massive energy consumption. As the scale of the aluminum electrolysis industry continues to expand, its energy consumption has become increasingly prominent [1–3]. Increasing the current of the electrolytic cell series can improve current efficiency, so the super-large-scale aluminum electrolytic cell with high current intensity is becoming the development trend of electrolytic cell design and development [4,5]. As a current conductor, the busbar runs long and has a very high current intensity. The distribution of the electro-thermal field of the busbar system directly affects the stability of electrolysis production and operating costs. On the one hand, the high current intensity in the busbar makes the physical fields in the electrolytic cell more complicated. On the other hand, the high current intensity increases heat generation of the busbar and changes the voltage drop, directly affecting the direct-current power consumption [6,7]. Therefore, accurately obtaining the electro-thermal field distribution of the busbar system holds significance for guiding the development and optimization of the busbar configuration of the super-large-scale aluminum electrolytic cell, as well as its energy-saving and stable operation.

For a long time, the busbar design mainly started from the perspective of optimizing the magnetic field distribution. By optimizing the busbar configuration, the disturbance growth rate of melt fluctuations is reduced, and the stability of the electrolytic cell is improved [8]. Most research focused on the influence of busbar configuration on the current distribution [9], magnetic field distribution [10] and magnetohydrodynamic [11–13], as

well as the distribution law of the electro-thermal fields of the whole cell [14–16]; however, there are few studies on the electro-thermal state of the busbar system.

Whitfield et al. [17] analyzed the electro-thermal state of the busbar after increasing the current intensity, and it is believed that the section area should be increased when the temperature of the busbar rises. Schneider et al. [18] numerically simulated the electro-thermal performance of busbars systems and found that busbar design has essential effects on the reliability of these systems. Zhou et al. [19] simulated the electro-thermal characteristics of the short-circuit busbar when it is in the electro-thermal equilibrium state. Qi et al. [20] established an electro-thermal coupling model to simulate the electrical equilibrium state of a single riser busbar. Necheporenko et al. [21] simulated the temperature distribution of a busbar system and found high temperature spots that required correction to avoid overheating. Ban et al. [22] performed calculations on thermoelectric busbar coupling and achieved good busbar techno-economic parameters. Szulborski et al. [23] developed a simulation model of physical–thermal phenomena occurring during the flow of current through current circuits and analyzed the temperature distribution in busbars during rated current flow. Garić et al. [24] simulated the steady-state heat transfer in and around rectangular bus bars installed horizontally in an indoor environment, considering the effects of horizontal transverse vibrations caused by electromagnetic forces.

However, the above studies are either based on the part of the busbar system or ignore the influence of the thermal state of the external environment. Especially with the development of the super-large-scale aluminum electrolytic cell, the current intensity increases greatly, which is particularly important for the design of the electro-thermal field of the busbar system. The influence of external conditions, such as ambient temperature and convective heat transfer coefficient, on the electro-thermal distribution of busbar systems has not been thoroughly studied. Thus, it is necessary to conduct a comprehensive and accurate calculation and analysis of the electro-thermal field distribution of the overall busbar system.

In this paper, the overall busbar system (excluding the anode busbar) in a 500 kA super-large-scale aluminum electrolytic cell was selected as the research object. The electro-thermal coupling calculation model of the busbar was established to simulate the electro-thermal field distribution. The characteristics of the busbar's current density, temperature, and voltage drop at different positions were explored. The effects of current intensity, ambient temperature, and surface heat transfer coefficient on the electro-thermal field distribution of the busbar were analyzed.

## 2. Model Description

### 2.1. Physical Model

According to the design drawings of the 500 kA aluminum electrolytic cell busbar system, the busbar system was established, including the cathode busbar, the riser busbar, and the cathode soft belt. The calculation region was divided into hexahedral element through sweeping, and the key areas were refined to make the calculation results of the model more realistic. The computational mesh consists of 758,924 elements and 1,066,074 nodes. The geometrical model is shown in Figure 1 and some typical key parameters are shown in Table 1.

The cathode busbar configuration is shown in Figure 2. The number of the riser busbar from left to right is 1 to 6. Riser busbar No. 1 is close to the duct end (DE), and riser busbar No.6 is close to the tapping end (TE). The numbers of soft belts connected to each riser busbar from left to right on the power inlet side are represented by  $a_1$ ,  $a_2$ ,  $a_3$ ,  $a_4$ ,  $a_5$ , and  $a_6$ , and the numbers of soft belts connected to each riser busbar from left to right on the power outlet side are represented by  $b_1$ ,  $b_2$ ,  $b_3$ ,  $b_4$ ,  $b_5$ , and  $b_6$ .

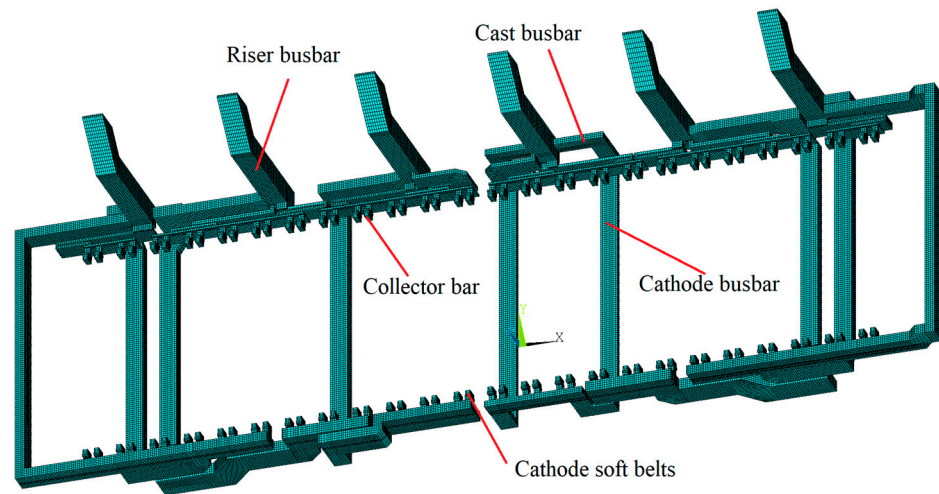


Figure 1. Geometrical model.

Table 1. Typical key parameters of the busbar system.

Busbar System	Cross-Sectional Area (m <sup>2</sup> )	Length (m)
Riser busbar	0.250	2.750
Collector bar (exposed part)	0.030	0.540
Cathode busbar	0.195	6.130
Cathode soft belt	0.010	0.276
Cast busbar	0.028	2.935

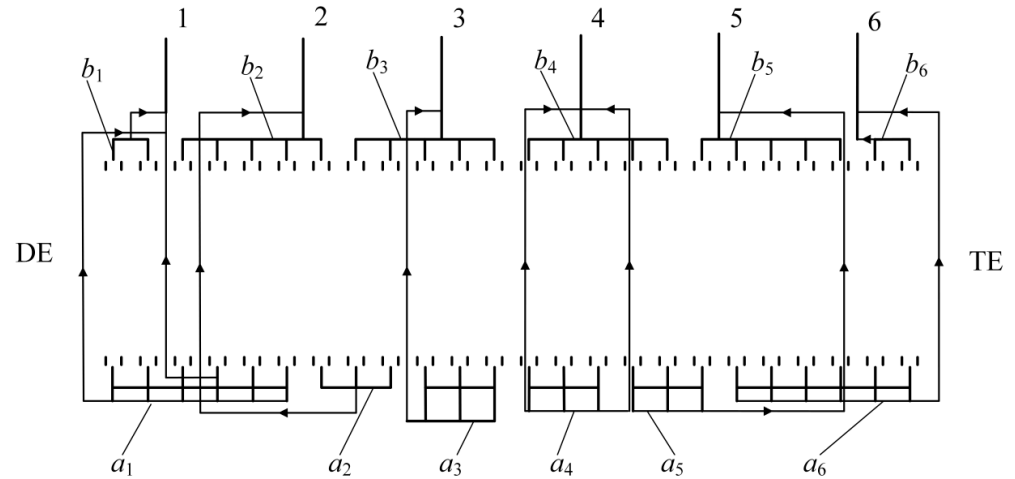


Figure 2. Diagram of the busbar configuration.

2.2. Governing Equation

The current flowing through the collector bar, cathode soft belt, cathode busbar, and riser busbar can be calculated according to Kirchhoff’s law:

$$\sum U = \sum I \cdot R \tag{1}$$

where  $U$  is the scalar voltage potential;  $I$  is the current;  $R$  is the resistance.

Electric conduction differential equation:

$$\delta_x \frac{\partial^2 U}{\partial x^2} + \delta_y \frac{\partial^2 U}{\partial y^2} + \delta_z \frac{\partial^2 U}{\partial z^2} = 0 \tag{2}$$

where  $\delta_x, \delta_y, \delta_z$  are the electrical conductivity in the X-axis, Y-axis and Z-axis, respectively.

Thermal conduction differential equation:

$$\frac{\partial}{\partial x} \left( k_x \frac{\partial T}{\partial x} \right) + \frac{\partial}{\partial y} \left( k_y \frac{\partial T}{\partial y} \right) + \frac{\partial}{\partial z} \left( k_z \frac{\partial T}{\partial z} \right) + q_s = 0 \quad (3)$$

where  $T$  is the temperature;  $k_x, k_y, k_z$  are the thermal conductivity in the X-axis, Y-axis, and Z-axis, respectively;  $q_s$  is the volume power of heat sources in the busbar.

The heat exchange between the busbar and the surroundings can be calculated by Newton's cooling formula:

$$q = \alpha(T_w - T_A) \quad (4)$$

where  $\alpha$  is the convective heat transfer coefficient;  $T_A$  is the temperature of the surrounding air;  $T_w$  is the surface temperature of the busbar.

The thermal radiation between the busbar and the surroundings can be calculated using the Stefan–Boltzmann law:

$$q = \varepsilon\sigma(T_w^4 - T_A^4) \quad (5)$$

where  $\sigma$  is the Stefan–Boltzmann constant,  $5.667 \times 10^{-8} \text{ W}\cdot\text{m}^{-2}\cdot\text{K}^{-4}$ ;  $\varepsilon$  is the emissivity of the busbar, which is 0.3.

### 2.3. Boundary Conditions

#### (1) Electrical boundary condition

The top section of the riser busbar is selected as the reference potential, that is, the zero-potential surface. The current through each collector bar is equally distributed according to the total current. The contact resistance at the busbar connection is ignored.

#### (2) Thermal boundary condition

The top section of the riser busbar is set as an adiabatic surface. The surface temperature of the collector bar and the ambient temperature around the busbars at different positions are the measured value. The surface heat transfer coefficient of the busbar can be expressed as [19]:

$$\alpha_{wA} = \alpha + \sigma\varepsilon(T_w^4 - T_A^4)/(T_w - T_A) \quad (6)$$

where  $\alpha_{wA}$  is the surface heat dissipation coefficient of the busbar.

The heat dissipation conditions of the busbar in different locations are different, and the values of the convection heat transfer coefficient  $\alpha$  are also different.

For the horizontal upward surface of the busbar:

$$\alpha = 1.31 \cdot k_1 \cdot (T_w - T_A)^{1/3} \quad (7)$$

For the horizontal downward surface of the busbar:

$$\alpha = 0.58 \cdot k_2 \cdot (T_w - T_A)^{1/3} \quad (8)$$

For the vertical surface (no occlusion on the side):

$$\alpha = 1.31 \cdot k_3 \cdot (T_w - T_A)^{1/3} \quad (9)$$

For the vertical surface (with occlusion next to it):

$$\alpha = 1.31 \cdot k_4 \cdot (T_w - T_A)^{1/3} \quad (10)$$

For the horizontal downward surface in contact with the supporting pier:

$$\alpha = 1.31 \cdot k_5 \cdot (T_w - T_A)^{(1/3)} \quad (11)$$

For the contact surface of the cathode busbar and cathode soft belt:

$$\alpha = 1.52 \cdot k_6 \cdot (T_w - T_A)^{1/3} \quad (12)$$

In Equations (7)–(12),  $k_1$ ,  $k_2$ ,  $k_3$ ,  $k_4$ ,  $k_5$ , and  $k_6$  are the correction coefficients of the heat transfer coefficient of various surfaces, which are obtained through repeated simulations according to the measured temperature values. Firstly, assuming a heat transfer coefficient, the temperature of the busbar can be simulated. The calculated results are then compared with the measured results. According to the comparison results, the heat transfer coefficient is modified and calculated repeatedly. Finally, the heat transfer coefficients can be obtained when the difference between the calculated results and the measured results is within the allowable range. The correction coefficients are shown in Table 2.

**Table 2.** Correction coefficients of the heat transfer coefficient.

Correction Coefficients	$k_1$	$k_2$	$k_3$	$k_4$	$k_5$	$k_6$
Values	3.0	1.4	1.0	2.5	0.3	4.2

### 3. Results and Discussion

#### 3.1. Mesh Independency Study

In total, four finite element meshes with different number of elements are used for the mesh independence tests and the simulation results are shown in Table 3. The numbers of finite elements are 512,786, 758,924, 1,199,094, and 1,654,458, respectively. The simulation results show minimal changes in the temperature of the riser busbars and cast busbars when the number of finite elements is larger than 758,924. This indicates that the mesh used can meet the requirement of the calculation.

**Table 3.** Mesh independence verification.

Location	Temperature (°C)			
	512,786 Elements	758,924 Elements	1,199,094 Elements	1,654,458 Elements
Riser busbar 1	92.1	90.9	90.4	90.3
Riser busbar 2	111.4	110.1	109.6	109.4
Riser busbar 3	116.5	115.5	115.2	115.0
Riser busbar 4	119.9	118.8	118.4	118.2
Riser busbar 5	104.0	103.1	102.8	102.7
Riser busbar 6	84.5	83.8	83.5	83.3
Cast busbars 1	139.8	138.5	138.1	137.9
Cast busbars 2	149.3	147.6	147.3	147.0
Cast busbars 3	152.1	150.2	149.8	149.6
Cast busbars 4	158.7	156.5	156.1	155.9
Cast busbars 5	145.2	143.0	142.6	142.3
Cast busbars 6	126.9	125.8	125.5	125.3

#### 3.2. Model Validation

Figure 3 shows the temperature distribution of the busbar system. As can be seen from Figure 3, the temperature distribution of the busbar system is higher in the middle and gradually decreases along the direction of the tapping end and the direction of the duct end from the middle. The average temperature of the No. 3 and No. 4 riser busbars in the middle is the highest, and the temperature ranges between 108.1 °C and 126.1 °C, which is basically in line with the actual situation of aluminum electrolysis production. In order to verify the accuracy of our model, the temperature values of the riser busbars and the cast busbars on side B were extracted by using ANSYS self-compiled program, and the thermal field calculation results were compared with the measured data of a 500 kA aluminum electrolytic cell, as shown in Tables 4 and 5.

The measured value is tested by a surface thermocouple. The dust on the surface of the measuring point of the busbar is removed before measurement, and then the surface thermocouple is attached to the measuring position to obtain the measured temperature value. For the riser busbar and cast busbar, the temperatures are measured at intervals of 30 cm. The measured data in Tables 4 and 5 are the average values of these measurements of riser busbar and cast busbar.

By comparing the calculated and measured average temperature values of each riser busbar in Table 4, it can be found that the average temperature of each riser busbar is basically consistent with the actual situation. The error between the calculated and measured values can be calculated as follows:

$$E_{error} = (T_M - T_{cal})/T_M \quad (13)$$

where  $E_{error}$  is error,  $T_M$  is the measured value, and  $T_{cal}$  is the calculated value.

Through calculation, the errors are within 8%, which is within a reasonable range. Numbers 1 to 6 in Table 5 represent the cast busbars on side B connected to the riser busbars from No. 1 to No. 6, respectively. By comparing the calculated and measured average temperatures of cast busbars on side B, it is found that their results are basically consistent with an error of less than 6%. Therefore, the model established in this paper accurately calculates the busbars' temperature distribution.

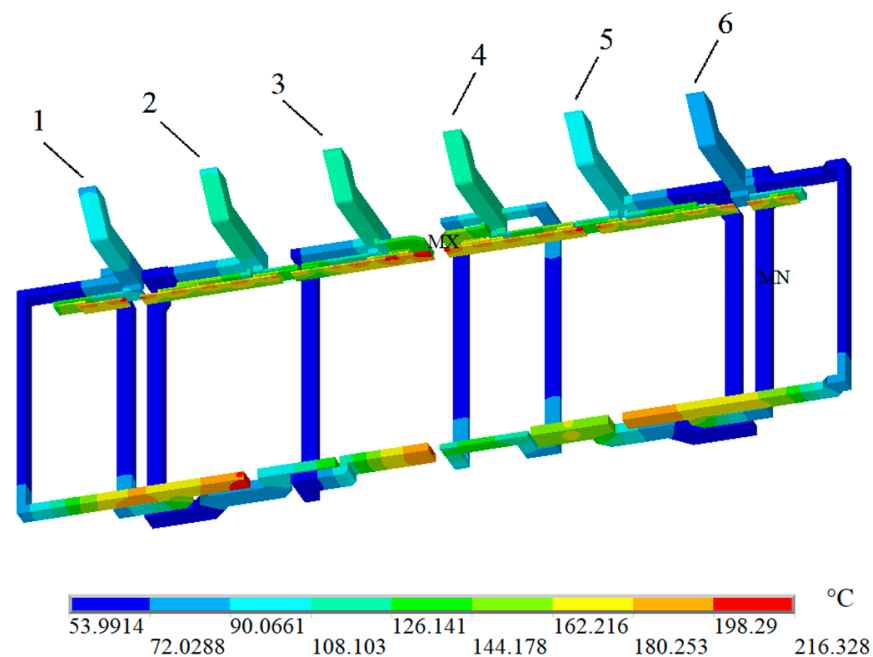


Figure 3. Temperature distribution of the busbar system.

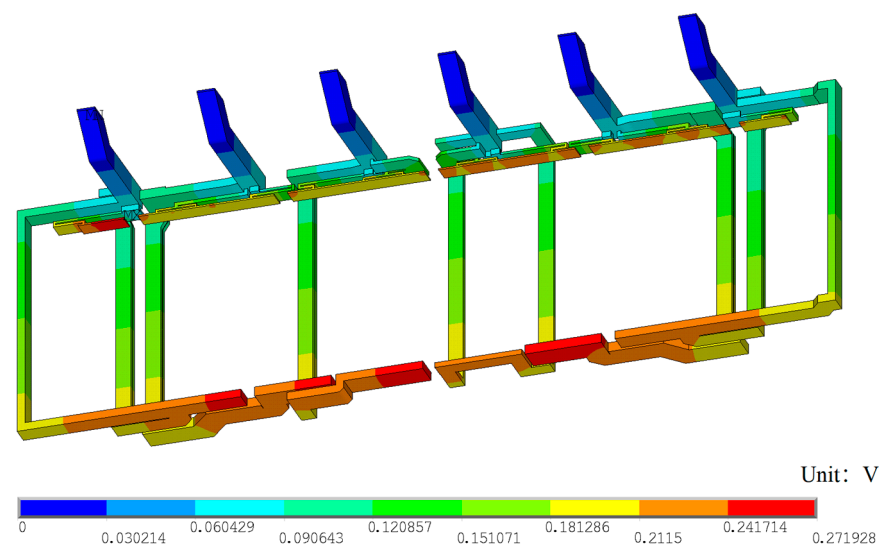
Table 4. Comparison of calculated and measured temperatures of the riser busbars.

Number	Calculated Value (°C)	Measured Value (°C)	Error (%)
1	90.9	98.5	7.7
2	110.1	115.1	4.3
3	115.5	119.5	3.3
4	118.8	123.5	3.8
5	103.1	106.5	3.2
6	83.8	86.4	3.0

**Table 5.** Comparison of calculated and measured temperatures of the cast busbars.

Number	Calculated Value (°C)	Measured Value (°C)	Error (%)
1	138.5	133.5	2.8
2	147.6	140.4	5.1
3	150.2	142.0	2.4
4	156.5	153.5	3.9
5	143.0	138.2	3.5
6	125.8	121.0	4.0

Figure 4 shows the potential distribution of the busbar system. It can be seen that the voltage drop of the entire busbar system is about 271.9 mV, which is close to the measured busbar voltage drop of 287.6 mV, with an error of 2.3%. Our model is also proved accurate in calculating the electric field distribution.

**Figure 4.** Voltage distribution of the busbar system.

### 3.3. Analysis of the Electro-Thermal Field of the Busbars System

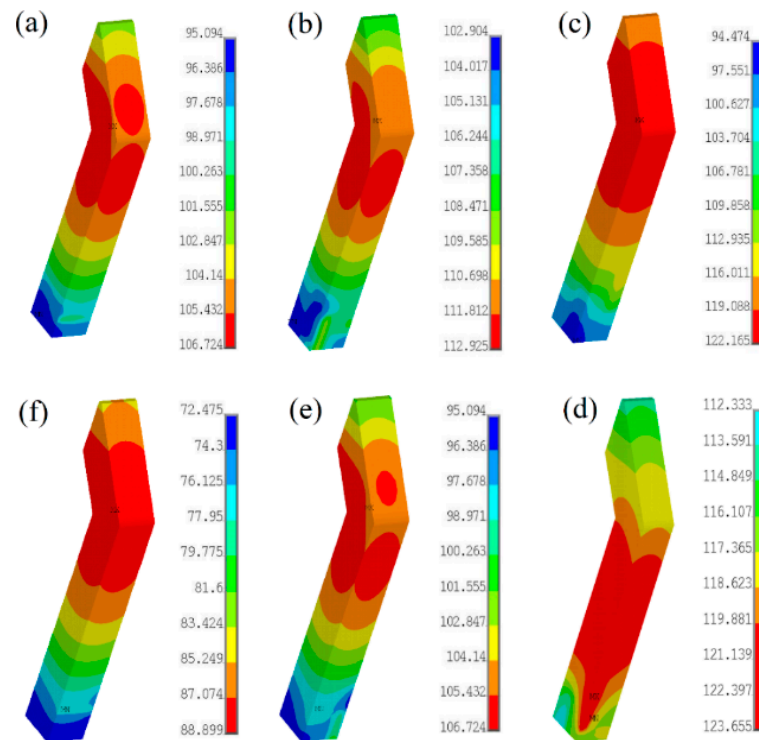
#### 3.3.1. Riser Busbar

The current density, voltage drop, and average temperature of the six riser busbars are shown in Table 6. It can be seen that the current density of the six riser busbars differ, among which the No. 6 riser busbar is the lowest with  $0.296 \text{ A/mm}^2$ , and the No. 1 riser busbar is the highest with  $0.328 \text{ A/mm}^2$ . However, the average temperature of the No. 1 riser busbar is relatively low. Comparing No. 3, No. 5 and No. 6 riser busbars of the same length, it is found that the voltage drop of the busbars with high current density is obviously higher, but the temperature of the busbars does not meet this characteristic. In the busbar system, the current density of the riser busbar is low, which shows that the change in heat generated by the change in current density is not enough to change the temperature value of the riser busbar significantly, but an increase in current density can increase the voltage drop of the busbar.

Figure 5 shows the temperature distribution characteristics of the riser busbars. As shown in Figure 5, the highest temperature points appear at the inner intersection of the vertical busbar and the oblique busbar, except for the No. 4 riser busbar. The highest temperature of the No. 4 riser busbar appears at the junction of the lower side. This is because there are more cast busbars connected to the riser busbar here, and the current is collected here with a large current density, which generates more Joule heat, resulting in local high temperature.

**Table 6.** Current density, voltage drop and average temperature of riser busbars.

Number of Riser Busbar	Current Density (A/mm <sup>2</sup> )	Voltage Drop (mV)	Average Temperature (°C)	Length of Riser Busbar (m)
1	0.328	75.1	90.9	3.94
2	0.324	84.4	110.1	4.19
3	0.311	80.6	115.5	4.10
4	0.326	80.0	118.8	3.83
5	0.327	85.0	103.1	4.10
6	0.296	70.2	83.8	4.10

**Figure 5.** Temperature distribution of the riser busbars: (a) No. 1 riser busbar; (b) No. 2 riser busbar; (c) No. 3 riser busbar; (d) No. 4 riser busbar; (e) No. 5 riser busbar; (f) No. 6 riser busbar.

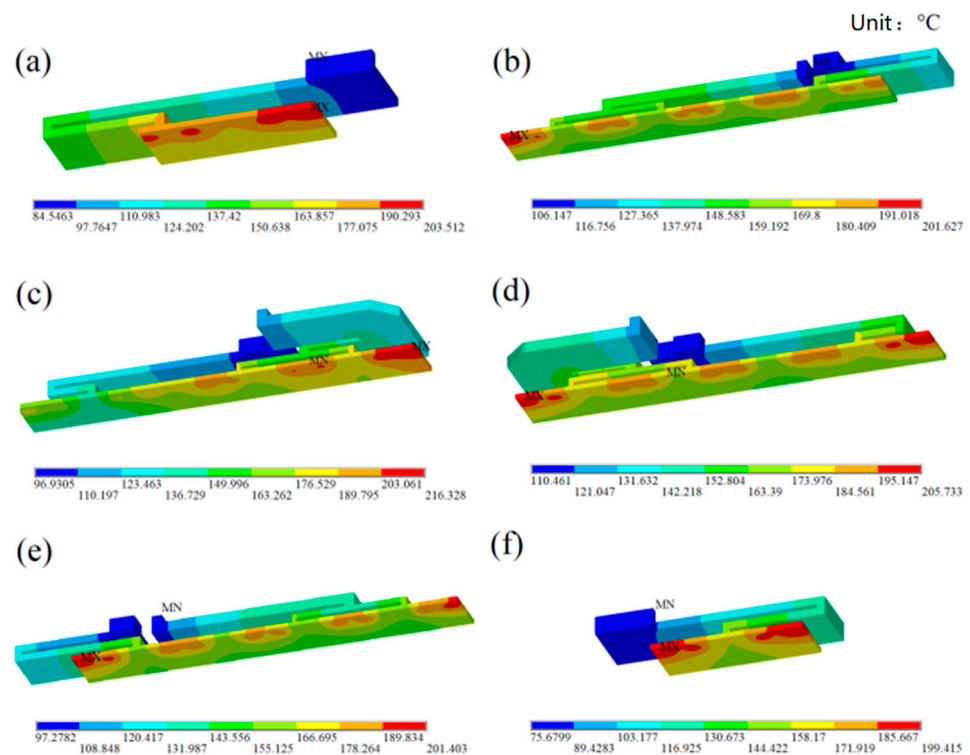
### 3.3.2. Cast Busbar

Table 7 shows the current density, voltage drop, and average temperature of the cast busbar on side B. As can be seen from Table 7, the current density of the cast busbar is generally large, about twice that of the riser bus. The average temperature of the cast busbar with a higher current density is lower than that of the cast busbar with a lower current density. This indicates that the main factors affecting the distribution of the electro-thermal field of the busbar are caused by differences in heat conduction and heat dissipation environment, while the Joule heat of the current is not the major factor.

**Table 7.** Current density, voltage drop and average temperature of cast busbar on side B.

Number of Riser Busbar	Current Density (A/mm <sup>2</sup> )	Voltage Drop (mV)	Average Temperature (°C)
1	0.652	200.4	138.5
2	0.582	149.6	148.9
3	0.561	150.2	150.2
4	0.546	153.4	156.5
5	0.588	144.4	143.0
6	0.621	146.5	125.8

Figure 6 shows the temperature distribution cloud map of the cast busbars on side B. It can be seen that the temperature of the cast busbar in contact with the cathode soft belt is significantly higher than that of other uncontacted cast busbars. In actual production, it can strengthen the heat dissipation of the end face of the cast busbar connected with the cathode soft belt to reduce the temperature and the voltage drop. In addition, the contact surface is not the place with the highest current density, and the conduction of heat from the cathode soft belt is the main factor affecting the temperature distribution of the cast busbar.



**Figure 6.** Temperature distribution of cast busbars on side B: (a) No. 1 cast busbar; (b) No. 2 cast busbar; (c) No. 3 cast busbar; (d) No. 4 cast busbar; (e) No. 5 cast busbar; (f) No. 6 cast busbar.

### 3.4. Effects of Parameters on Electrothermal Distribution of the Busbar

The analysis of the above simulation results shows that the distribution of the electro-thermal field of the busbar is closely related to the current intensity, ambient temperature, and surface heat transfer coefficient. In practice, the heat dissipation conditions of the busbars located in different positions of the aluminum reduction cell are different, which affects the current efficiency. In this paper, the change in electro-thermal state of the busbar was investigated under different current intensities, ambient temperatures and surface heat transfer coefficients.

#### 3.4.1. Effect of Current Intensity

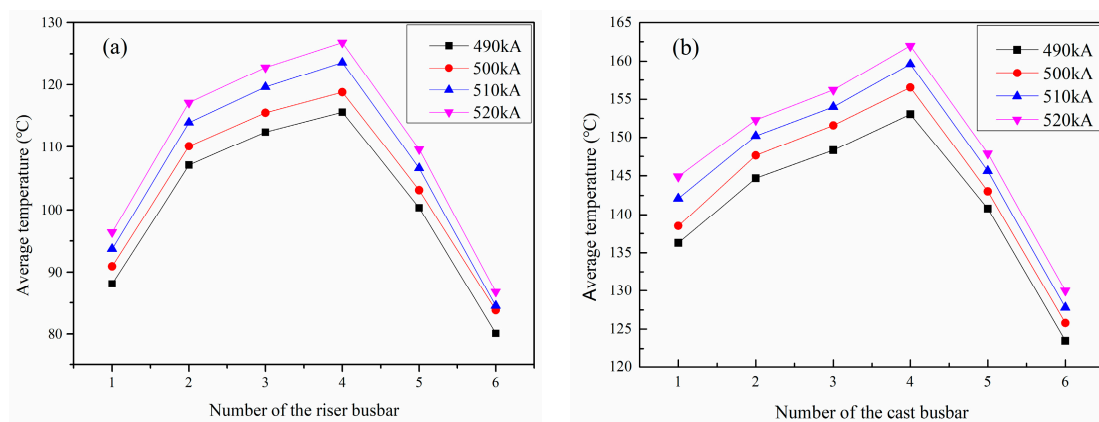
In order to understand the influence of current change on the distribution characteristics of the busbar system's electro-thermal field, currents of 490 kA, 510 kA, and 520 kA were simulated. The average temperature and voltage drop changes are shown in Table 8. It can be seen that the average temperature and voltage drop increase with the increase in current intensity. Under the current intensities of 490 kA, 510 kA, and 520 kA, the average temperature increases of the busbar system are  $-1.8\%$ ,  $+1.5\%$ , and  $+3.1\%$ , respectively, and the voltage drop increases are  $-2.8\%$ ,  $+2.8\%$ , and  $+5.7\%$ , respectively.

Figure 7 shows the temperature changes of the busbars under different current intensities. As can be seen from Figure 7a, with the increase in current intensity, the temperature rise of the riser busbar with high temperature is more evident than that of the riser busbar with low temperature, which further increases the temperature difference between the

riser busbars. The maximum temperature difference between riser busbars increases from 35.5 °C at 490 kA to 40.0 °C at 520 kA. As seen from Figure 7b, when the current increases, the temperature rise of the cast busbars on side B is generally linear. Because the current density of the cast busbar is larger than that of the riser busbar, the temperature variation amplitude is not as sensitive as that of the riser busbar.

**Table 8.** Variation in average temperature and voltage drop of busbar with current intensity.

Current Intensity (ka)	Busbar Temperature (°C)	Increase Amplitude (%)	Busbar Voltage Drop (mv)	Increase Amplitude (%)
490	106.1	−1.8	264.9	−2.8
500	108.0	0	272.6	0
510	109.6	1.5	280.1	2.8
520	111.3	3.1	288.2	5.7



**Figure 7.** Variation in busbar temperature with current at different locations: (a) riser busbar; (b) cast busbar on side B.

### 3.4.2. The Effect of Ambient Temperature

In order to investigate the influence of ambient temperature on the electro-thermal distribution of busbars, the electro-thermal field distribution of the busbars system under ambient temperatures of 30 °C, 50 °C, and 60 °C were simulated. When the ambient temperature changes, the average busbar temperature, and voltage drop change as shown in Table 9. As can be seen from Table 9, the average temperature and voltage drop of the busbar system increase with an increase in the ambient temperature. Compared with the electro-thermal field at an ambient temperature of 40 °C, it is found that under the ambient temperatures of 30 °C, 50 °C and 60 °C, the average temperature change range is −9.4%, +9.0%, and +17.9%, while the voltage drop change range is −2.9%, +2.8%, and +5.8%. The change in temperature rise is more significant than that of voltage.

Figure 8 shows the change in average busbar temperature at different positions with the ambient temperature. As seen from Figure 8, with the increase in ambient temperature, the average temperature of the riser busbar and the cast busbar on side B shows a linear increase trend. The change in average temperature of the cast busbar is smaller than that of the riser busbar. When the ambient temperature increases by 10 °C, the cast busbar temperature increases by 9.3 °C on average, while the riser busbar temperature increases by 12.3 °C on average. Because the cast busbar has a higher temperature and a smaller external area, it experiences less heat exchange with the surrounding environment, so its temperature rise is smaller than that of the riser bus.

**Table 9.** Variation in average temperature and voltage drop of busbar with ambient temperature.

Ambient Temperature (°C)	Busbar Temperature (°C)	Increase Amplitude (%)	Busbar Voltage Drop (mV)	Increase Amplitude (%)
30	97.8	−9.4	264.6	−2.9
40	108.0	0	272.6	0
50	117.7	9.0	280.3	2.8
60	127.3	17.9	288.3	5.8

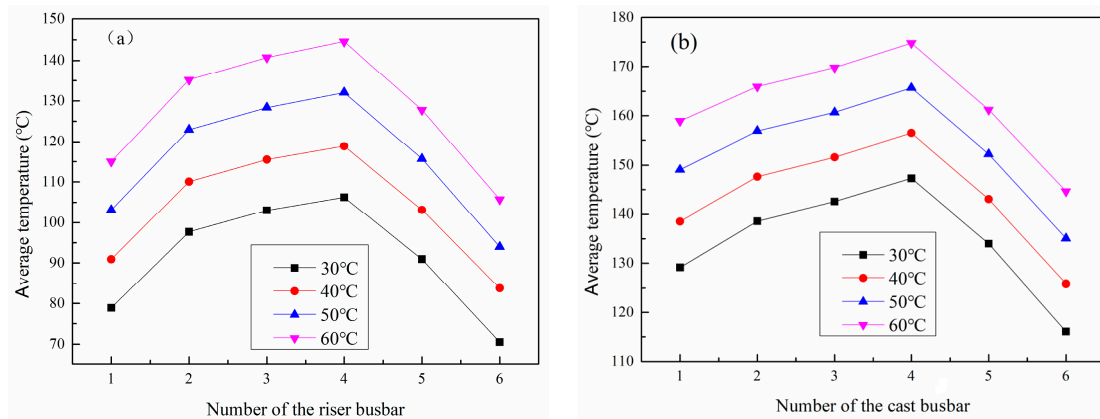


**Figure 8.** Variation in busbar temperature with ambient temperature at different locations: (a) riser busbar; (b) cast busbar on side B.

3.4.3. The Influence of Heat Transfer Coefficient

In order to study the influence of the heat transfer coefficient on the electro-thermal distribution, the heat transfer coefficient is reduced by 15%, increased by 15%, and increased by 30% compared with the base condition. The electro-thermal field distribution of the busbar was simulated. The average temperature and voltage drop of the busbar system after changing the heat transfer coefficient are shown in Table 10. It can be seen from Table 10 that the average temperature and voltage drop of the busbar system decreases with an increase in surface heat transfer coefficient. When the heat transfer coefficient decreases by 15%, increases by 15%, and increases by 30%, the average temperature of the busbar system changes by −9.4%, −8.1%, and −12.7%, and the voltage drop changes by +3.9%, −3.4%, and −5.4%. The change in temperature rise is more significant than that of voltage.

Figure 9 shows the change in the average temperature of the busbar at different positions with the heat transfer coefficient. It can be seen from Figure 9a that with the increase in heat transfer coefficient, the decreasing trend of the average temperature of the riser busbar is constantly slowing down. The higher temperature riser busbar is more affected by the heat transfer coefficient. As seen from Figure 9b, when the heat transfer coefficient increases, the average temperature of the cast busbar on side B decreases linearly.

**Table 10.** Variation in average temperature and voltage drop of busbar with heat transfer coefficient.

Heat Transfer Coefficient (%)	Busbar Temperature (°C)	Increase Amplitude (%)	Busbar Voltage Drop (mV)	Increase Amplitude (%)
−15%	118.1	+9.4	283.2	+3.9
Base condition	108.0	0	272.6	0
+15%	99.2	−8.1	263.3	−3.4
+30%	94.3	−12.7	257.9	−5.4

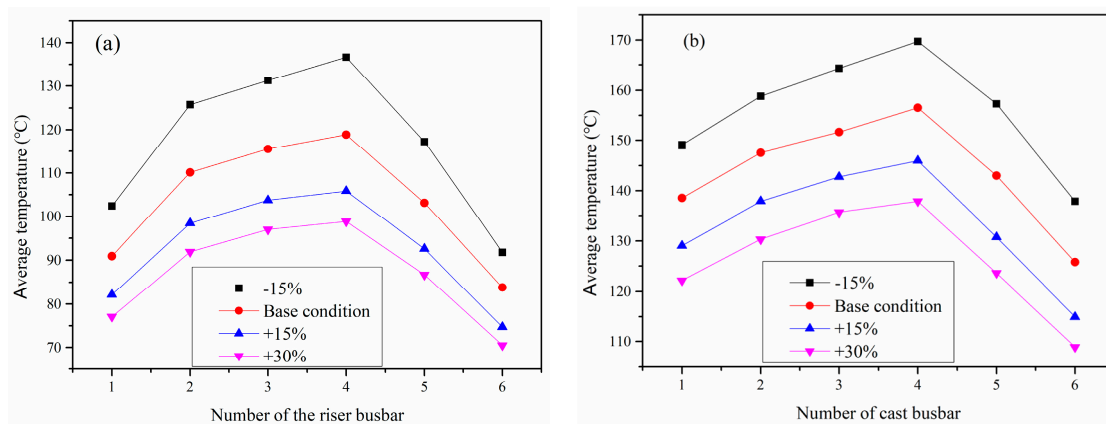


**Figure 9.** Variation in busbar temperature with heat transfer coefficient at different locations: (a) riser busbar; (b) cast busbar on side B.

#### 4. Conclusions

In this study, an electro-thermal coupling calculation model for the busbar system of a 500 kA super-large aluminum electrolytic cell was established. The model's accuracy was validated by comparing the simulation results with the measured values.

The temperature distribution of the riser busbar and the cathode busbar is higher in the central location, gradually decreasing from the center to both ends. Higher busbar temperature usually occurs at the contact point with the cathode soft belt.

The difference in heat conduction from the collector bar and the heat dissipation environment around the busbar is the main factor affecting the electro-thermal field distribution of the busbar, and the Joule heat of the current is not the main factor.

Compared with the base condition, when the current intensity increases to 520 kA, the changes in average temperature and voltage drop of the busbar system are +3.1% and +5.7%, respectively. When the ambient average temperature increases to 60 °C, the changes in average temperature and voltage drop of the busbar system are +17.9% and +5.8%, respectively. When the heat transfer coefficient increases by 30%, the changes in average temperature and voltage drop of the busbar system are −12.7% and −5.4%, respectively. Moreover, the influence rules of each factor on the electro-thermal state of the busbars at different positions are inconsistent.

**Author Contributions:** Conceptualization, W.H. and M.L.; methodology, W.H. and S.S.; software, W.H., K.S. and S.S.; validation, S.S. and M.L.; formal analysis, K.S.; investigation, S.S.; resources, M.L.; data curation, W.H.; writing—original draft preparation, W.H.; writing—review and editing, K.S. and M.L.; visualization, S.S.; supervision, M.L.; project administration, M.L.; funding acquisition, W.H. All authors have read and agreed to the published version of the manuscript.

**Funding:** This research is supported by the Fundamental Research Program of Shanxi Province (202203021222028) and the Fundamental Research Funds for the Central Universities of Central South University (2018zzts157).

**Data Availability Statement:** Data sharing is not applicable.

**Conflicts of Interest:** The authors declare no conflict of interest.

#### References

1. Yang, Y.; Guo, Y.Q.; Zhu, W.S.; Huang, J.B. Environmental impact assessment of China's primary aluminum based on life cycle assessment. *Trans. Nonferrous Met. Soc. China* **2019**, *29*, 1784–1792. [[CrossRef](#)]
2. Lin, B.; Xu, L. Energy conservation of electrolytic aluminum industry in China. *Renew. Sustain. Energy Rev.* **2015**, *43*, 676–686. [[CrossRef](#)]
3. Hou, W.Y.; Li, H.S.; Li, M.; Cheng, B.J.; Feng, Y. Effects of electrolysis process parameters on alumina dissolution and their optimization. *Trans. Nonferrous Met. Soc. China* **2020**, *30*, 3390–3403. [[CrossRef](#)]

4. Li, H.; Wang, J.; Hou, W.; Li, M.; Cheng, B.; Feng, Y.; Xu, T. The study of carbon recovery from electrolysis aluminum carbon dust by froth flotation. *Metals* **2021**, *11*, 145. [[CrossRef](#)]
5. Zhang, H.L.; Liang, J.D.; Li, J.; Sun, K.N.; Xiao, J. Evolution of the busbar structure in large-scale aluminum reduction cells. *JOM* **2016**, *69*, 307–314. [[CrossRef](#)]
6. Li, J.; Zhang, H.L.; Xu, Y.J. Simulated computation and optimization of comprehensive physical fields in modern large-scale aluminium reduction cells. *Chin. J. Trans. Nonferrous* **2011**, *21*, 2594–2606.
7. Li, M.; Zhou, J.M. Numerical simulation of busbar configuration in large aluminum electrolysis cell. *J. Cent. South Univ. Technol.* **2008**, *15*, 271–275. [[CrossRef](#)]
8. Yang, Q. Development and outlook for busbar arrangement of aluminum reduction pots. *Light Met.* **2019**, *9*, 36–39.
9. Kacprzak, D.; Gustafsson, M.; Li, L.; Taylor, M. *Numerical Analysis of the Collector Bar Current Distribution of a Reduction Cell*; Galloway, T.J., Ed.; Light Metals: Warrendale, PA, USA, 2006; pp. 367–371.
10. Li, M.; Zhou, J.M. *Modeling and Optimization of Busbar Configuration in Aluminum Electrolysis Cells with Genetic Algorithm*; Johnson, J.A., Ed.; Light Metals: Warrendale, PA, USA, 2010; pp. 489–492.
11. Dupuis, M.; Bojarevics, V. *Weakly Coupled Thermo-Electric and MHD Mathematical Models of an Aluminium Electrolysis Cell*; Kvande, H., Ed.; Light Metals: Warrendale, PA, USA, 2005; pp. 449–454.
12. Ruan, S.Y.; Yan, F.Y.; Dupuis, M.; Bojarevics, V.; Zhou, J.F. *Production Application Study on Magneto-Hydro-Dynamic Stability of a Large Prebaked Anode Aluminum Reduction Cell*; Sadler, B.A., Ed.; Light Metals: Warrendale, PA, USA, 2013; pp. 603–607.
13. Pianykh, A.A.; Arkhipov, G.V.; Tretyakov, Y.A. Mathematical model of magnetic hydrodynamics and heat transfer in an aluminum reduction cell. *Russ. J. Non-Ferrous Met.* **2020**, *61*, 65–73. [[CrossRef](#)]
14. Sun, S.G.; Li, M.; Cheng, B.J.; Li, H.; Hou, W.Y. Industrial experimental research and temperature distribution in aluminum reduction cell. *J. Cent. South Univ.* **2020**, *51*, 872–881.
15. Allard, F.; Desilets, M.; Blais, A.A. Modeling approach for time-dependent geometry applied to transient heat transfer of aluminum electrolysis cells. *Metall. Mater. Trans. B* **2019**, *50*, 958–980. [[CrossRef](#)]
16. Xu, Y.J.; Li, J.; Yin, C.G.; Yang, S.; Zhang, H.L.; Lv, X.J. Method of strongly coupled modeling and computing for thermal-electrical field in aluminium reduction cells. *Chin. J. Trans. Nonferrous* **2014**, *24*, 239–245.
17. Whitfield, D.; Said, A.A.; Al-Jallaf, M.M.K.; Mohammed, A.H.A. *Development of D18 Cell Technology at Dubal*; Bearne, G., Ed.; Light Metals: Warrendale, PA, USA, 2009; pp. 477–481.
18. Schneider, A.F.; Richard, D.; Charette, O. *Impact of Amperage Creep on Potroom Busbars and Electrical Insulation: Thermal-Electrical Aspects*; Lindsay, S.J., Ed.; Light Metals: Warrendale, PA, USA, 2011; pp. 525–530.
19. Zhou, N.J.; Zhang, J.Q.; Zhou, S.H. Electric and thermal simulation for short circuit busbar of aluminum reduction cells. *J. Cent. South Univ.* **2010**, *41*, 1609–1615.
20. Qi, X.Q. Electro-thermal simulating and electric balance analysis for bus bars of large aluminium reduction cells. *Light Met.* **2012**, *12*, 29–34.
21. Necheporenko, I.; Arkhipov, A. Modelling of the magnetic field and magnetohydrodynamic behaviour of a typical aluminium cell using COMSOL. In Proceedings of the COMSOL Conference 2020 Europe Section, Cambridge, UK, 4 June 2020.
22. Ban, Y.; Mao, J.; Mao, Y.; Liu, J.; Chen, G. *Development and Industrial Application of NEUI600 High Efficiency Aluminum Reduction Cell*; Martin, O., Ed.; Light Metals: Warrendale, PA, USA, 2018; pp. 705–713.
23. Szulborski, M.; Łapczyński, S.; Kolimas, Ł. Thermal analysis of heat distribution in busbars during rated current flow in low-voltage industrial switchgear. *Energies* **2021**, *14*, 2427. [[CrossRef](#)]
24. Garić, L.; Klimenta, D.; Andriukaitis, D.; Jovanović, S. Modeling the effects of horizontal transverse vibrations on the thermal behavior and the ampacity of rectangular bus bars. *Appl. Sci.* **2023**, *13*, 6745. [[CrossRef](#)]

**Disclaimer/Publisher’s Note:** The statements, opinions and data contained in all publications are solely those of the individual author(s) and contributor(s) and not of MDPI and/or the editor(s). MDPI and/or the editor(s) disclaim responsibility for any injury to people or property resulting from any ideas, methods, instructions or products referred to in the content.